Correlations of Interlayer Time with Distortion of Large Ti-6Al-4V Components in Laser Metal Deposition with Wire

Y.S. Lee[a, b*], Y. Bandari[a, c], S. Simunovic[d], B. Richardson[a, c], M.M. Kirka[a, b]

a. Manufacturing Demonstration Facility, Oak Ridge National Laboratory, Knoxville, TN, USA
b. Materials Science and Technology Division, Oak Ridge National Laboratory, Oak Ridge, TN, USA
c. Energy Science and Transportation Division, Oak Ridge National Laboratory, Oak Ridge, TN, USA
d. Computational Sciences & Engineering Division, Oak Ridge National Laboratory, Oak Ridge, TN, USA

*Corresponding author: leey@ornl.gov

Keywords: LMD-wire, Distortion, Inter-layer time, Finite element method, Additive manufacturing, Plate oscillation, Ti-6Al-4V

Abstract

Laser metal deposition with wire (LMD-w) is one of the emerging additive manufacturing (AM) technologies for large-scale aerospace components due to high deposition rates and material efficiency. However, it often results in undesired stresses and distortions due to non-uniform expansion and contraction of material during printing. Controlling inter-layer time, preheating, and clamping are the effective methods to mitigate the thermally induced stress and deformation. In this study, the effect of inter-layer cooling time on part distortion is investigated using a finite element method (FEM). The model accounts for actual tool paths, power, and cooling conditions. The results show that the model effectively captures the fluctuation of the Ti-6Al-4V plate during printing. Also, it shows an asymmetric distortion on the plate edges. Ultimately, the sequentially coupled thermal-stress simulation provided a quantitative understanding of the inter-layer cooling time on titanium plate distortion for the large-scale LMD-w process.

1. Introduction

Laser metal deposition with wire (LMD-w) is one of the promising Direct Energy Deposition (DED) technologies. It is known as an ideal process for large component fabrication with moderate complexity since the wire-feeding method offers high productivity due to high deposition rates, material efficiency, and a less costly system. However, a few production challenges have not been fully resolved in large-scale LMD-w process [1].

A LMD-w system generally consists of a laser heat source equipped on a robotic arm, wire feeder, and accessorial systems (e.g., tables, shielding gas, and recording tools such as cameras and thermocouples). The laser and wire feeder are moved using an automatically controlled robotic arm. The laser heat source melts the substrate, and the metal wire feeder forms

a new deposit on the substrate. During printing, the material experiences multiple heating and cooling cycles. This induces thermal stress and distortion due to non-uniform expansion and contraction of the material because of the repeated heating and cooling. It also contributes to form residual stress, resulting in significant distortion after the part is unclamped.

Many researches have studied to find out an optimum control strategy for thermally induced stress, residual stress, and resultant distortion in the large part [2, 3]. Mughal et al. [4] investigated the effect of inter-layer time on the thermal stress and deformation using 2-D thermo-mechanical model. It was found that employing inter-layer cooling can reduce the part's deformation. Zhao [5] et al. also showed that both inter-layer stress and residual stress can be reduced by controlling inter-layer cooling time. Aggarangsi and Beuth [6] reported that uniform preheating reduces residual stress by a maximum of 18%. However, the inter-layer cooling time decreases the production rate, while preheating delivers excessive heat to the deposit particularly in continuous printing, resulting in undesirable remelting and poor surface finish. This indicates that a compromise should be made to find optimum process parameters.

Numerical simulations have been reported for large-scale AM processes. Ding [7, 8] developed a steady state Finite Element (FE) simulation to increase computational efficiency for the metal Big Area Additive Manufacturing (mBAAM) process. They showed that stress across thedeposit is uniform, but the significant residual stress develops after unclamping, which leads to large distortion. Montevecchi et al. [9] developed an FE simulation for mBAAM accounting for actual power distribution between filler wire and substrate material. They calculated the optimal inter-layer time to achieve constant inter-layer temperature and constant melt pool volume. Denlinger [10] developed an FE model using an adaptive coarsening method combined with an element birth and death technique to predict the distortion of large-scale part in electron mBAAM. Simunovic et al. [11] showed a simulation to predict a part's distortion for mBAAM considering actual tool path and energy information using finite element method (FEM). They successfully demonstrated a feasibility of the numerical modeling for a complex large excavator arm. Hence, an emphasis on AM process control has been required to mitigate (or eliminate) part distortion in large-scale titanium components including inter-layer time.

The aim of the study presented below is to demonstrate part scale heat transfer simulation in an LMD-w system and structural corresponds to large-scale part distortion. One of the key aspects of this work is to account for the actual tool path, power, and cooling conditions. The thermo-mechanical model is validated with in-situ temperature and layer by layer distortion measurement.

2. Experimentation

2.1. Laser metal deposition with wire

The experiment was carried out with a six-axis KUKA robot system. A fiber laser with a maximum power of 20.0 kW was used as the heat source for the LMD-w system. The laser was delivered to the work piece through an optical fiber. The laser spot diameter was 7.4 mm. The deposited material was fed from 1.6 mm Ti-6Al-4V wire with an Abicor Binzel wire feeder. The experiments were conducted in a closed argon environment with less than 250 ppm oxygen content. A laser line scanner was used to measure the bead height and plate distortion.

2.2. Experimental configuration and observation of the process

Configuration of LMD-w experiment consisted of a Ti wall, Ti plate, ceramic washer, steel plate, and Al plate as seen in Fig. 1(a). The wall height is11.0 mm for ten-layers of deposit. The Ti build plate was mounted on the ceramic washer with 2.54 mm thickness and fastened with the steel plate using medium carbon steel bolts with the washer. The bead width was 11.5 mm, and the double bead deposit was 9 mm center to center as seen in Fig. 1(b). The Ti plate's dimensions were 500 mm (length) x 155 mm (width) x 6.4 mm (thickness) as seen in Fig. 1(c). The thermocouples were placed with 100 mm spacing from each other on the Ti build plate marked as red spots in Fig. 1(c). The plate scan was implemented in every layer to measure the variation of the plate distortion. The measured plate distortion along A-B in Fig. 1(c) was used to validate simulation. Unidirectional scan strategy was used to create the 200 mm long deposits. The LMD-w station is shown in Fig. 1(d).

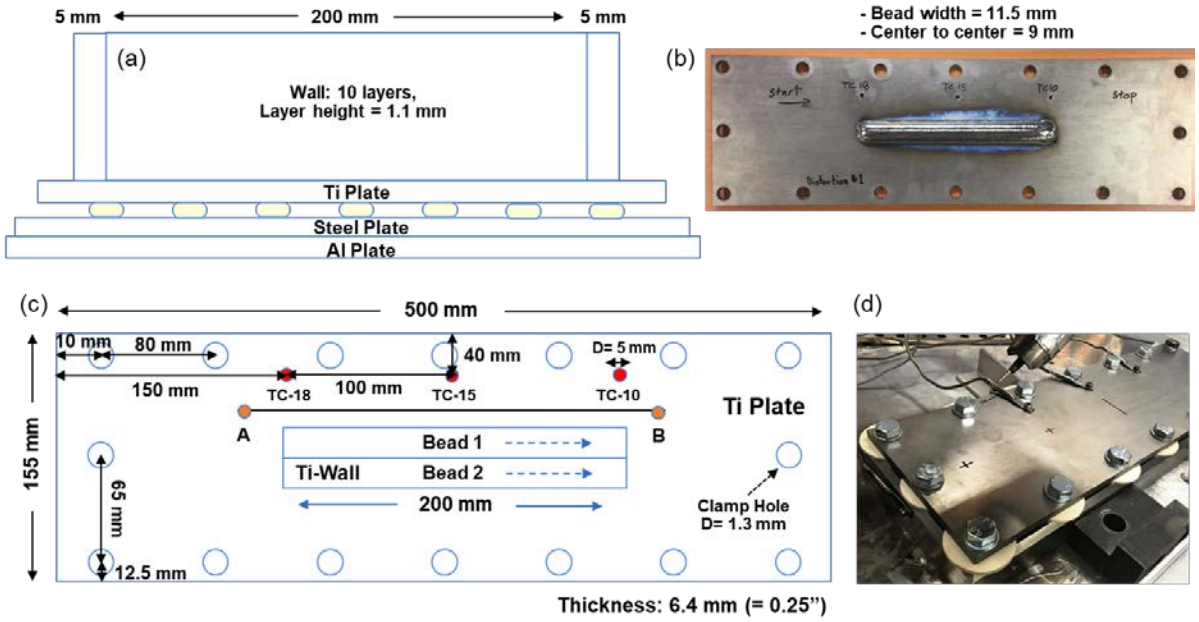

Figure 1. Build geometry: the LMD-w station consisted of Ti wall, Ti build plate, ceramic washer, steel plate, and Al plate. A bolt clamp was used to fix the Ti build plate to the steel plate.

Figure 2 shows the variation of laser power as a function of time during the build. The power surges as the laser beam is powered on and is maintained for approximately 42s to create

the first bead. Then, it returns to the start position for about 8s. While the robot head moves to the start position, the laser power surges instantaneously at after 2,330s and cuts the wire to maintain the constant wire length. The velocity of laser deaccelerates to zero as it approaches the edge where the first deposit occurs. Meanwhile, the wire keeps stretching even at zero velocity. Consequently, the wire length becomes longer than desired. Then, the beam is turned on for the second bead. The inter-layer time is estimated from the time interval between the second beam-off and third beam-on as illustrated in Fig. 2.

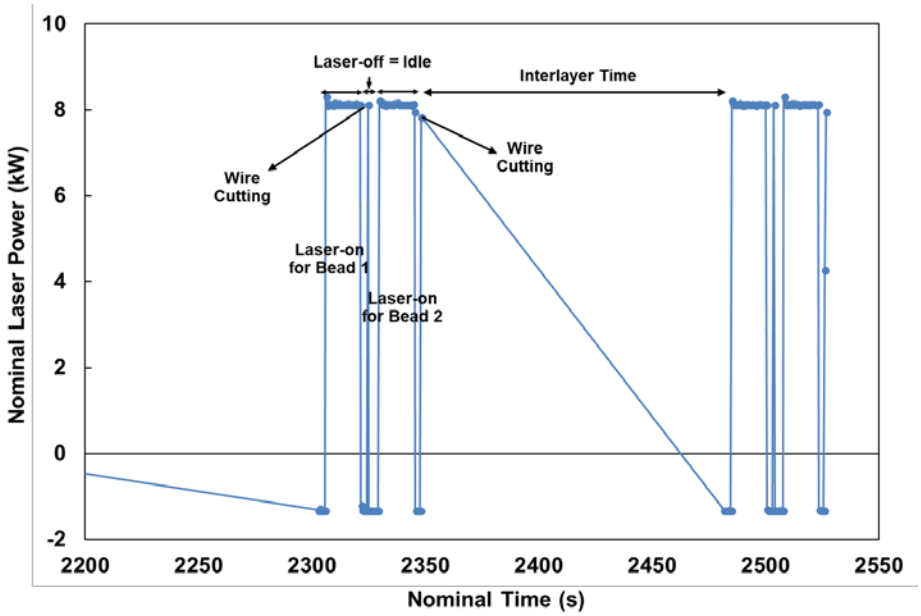

Figure 2. Estimation of inter-layer and bead time from the measurement of laser power.

Three different experimental settings were explored to investigate the relationship between inter-layer time and temperature profile. Build 1 was built with clamps attached all around the substrate with no pause time between layers. Build 2 was built with clamps attached all around the substrate, but a pause for about 30 minutes was taken after the fifth layer. Build 3 was built with only center clamps attached to the substrate and without pausing the laser. The estimated inter-layer time is plotted in Fig. 3 for the builds 1-3. The inter-layer time significantly varies with the number of layers and the build settings. The inter-layer time is set in the range of 91 to 200s. Generally, the inter-layer time is shorter at layers 1-5 and becomes longer at layers 6-10. This occurs because the temperature increases as the deposit builds up due to a characteristic thermal feature of thin walls. In other words, the direction of heat dissipation becomes dominant along the build direction, which causes the build temperature to increase as more layers are deposited on the plate. Therefore, longer inter-layer time is recommended for constant layer temperature.

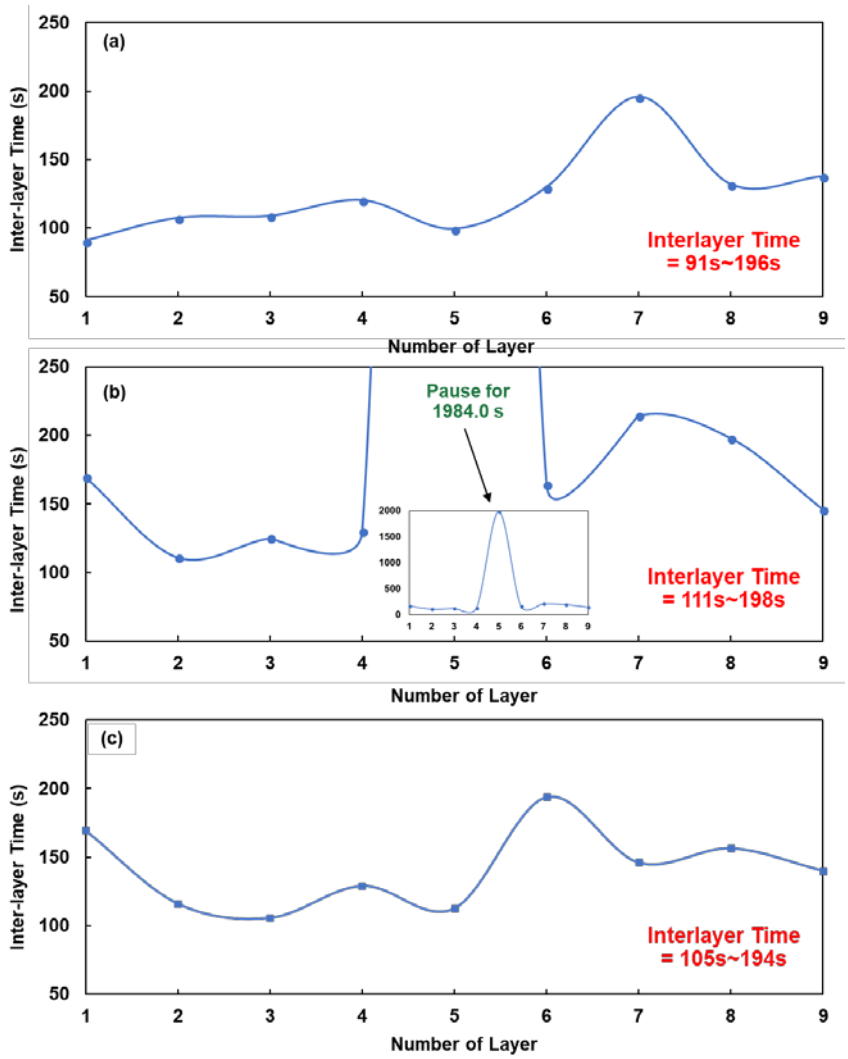

Figure 3 Estimated inter-layer time at (a) build 1 (=all clamps & no pause) (b) build 2 (=all clamps & a pause) (c) build 3 (=center clamps & no pause).

In Fig. 4, the temperature profile is measured at TC-10, 15, and 18 in builds 1-3. Temperature at the center (=TC-15) is approximately 100~130 ^{o}C higher than that at the left (=TC-18) and right (=TC-10) regions. In Fig. 4(d)-(f), there are two peak temperatures observed. These peak temperatures occur because there is about a 30-minute pause right after the 5th layer is deposited. The pause seems to significantly decrease overall temperature at the TCs. The peak temperature at the center of build 2 in Fig. 4(e) is about 80 ^{o}C lower than the peak temperatures of the same center region in Fig. 4(b) and (h). It was observed that the temperature profile is not symmetric on the left and right side of the plate. The salient, non-uniformity was found at the center clamped condition in Fig. (g) and (i). The difference in temperature is about 30 ^{o}C in build 3, whereas it is about 18 ^{o}C in the builds of 1 and 2. This implies that the bolt clamp leads to improved uniformity in temperature on the plate.

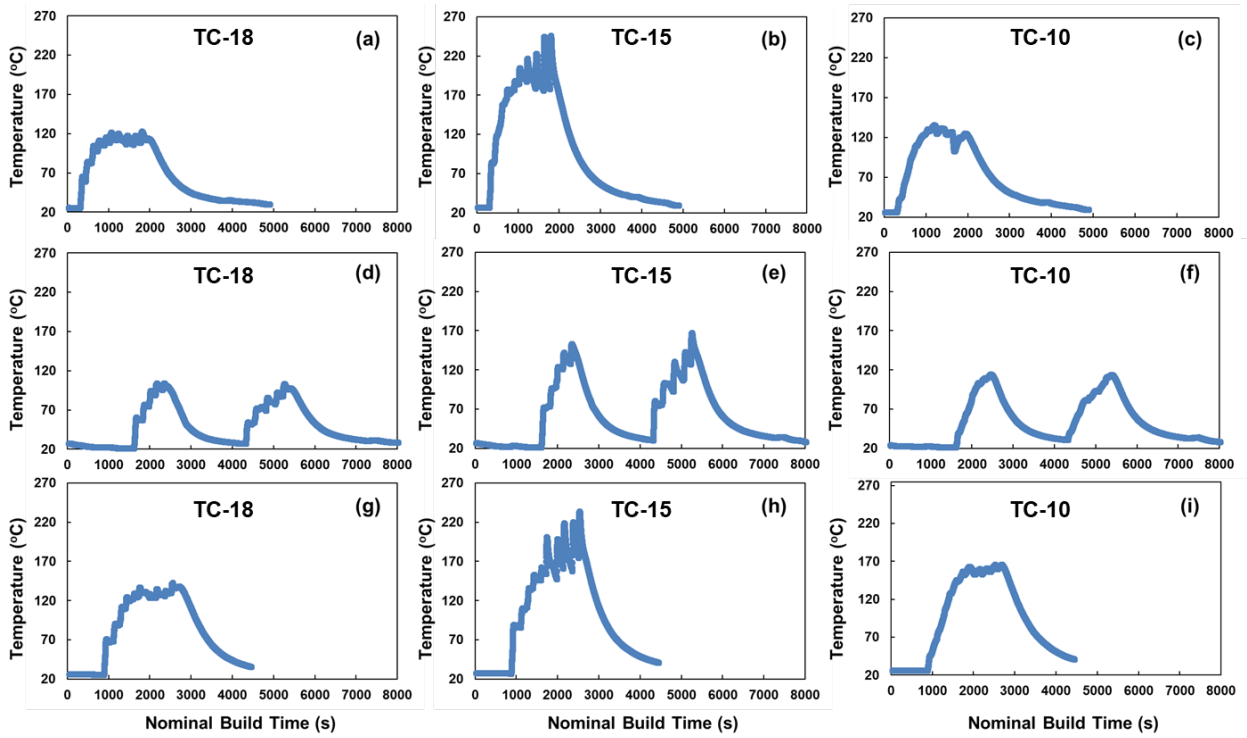

Figure 4. Measured temperature profile at TC-18, TC-15 and TC-10 in Fig. 1(c), (a)-(c): build 1 (=all clamp & no pause), (d)-(f): build 2 (center clamp & a pause) and (g)-(i) build 3 (=center clamp & no pause).

3. Model Development

The 3-D simulation was implemented based on the numerical solution of heat transfer equations. The governing equation was discretized and solved using commercial software, *Abaqus* [12], for heat transfer and stress analyses. The model was sequentially coupled with heat transfer-stress analysis such that it assumed that the temperature field was not influenced by phase transformation or mechanical deformation. The heat transfer simulation was first performed, and the transient temperature field obtained from the analysis was applied as a thermal load for the stress analysis. A progressive material activation method was used to describe the material addition of the wire. The Ti wall was inactive at the beginning of the simulation. Then, as the material deposition started, the elements were activated according to the actual path of the beam and wire. The laser power was integrated over time and beam travel distance in a specified time step, and then the integrated flux was incorporated into the active elements. The key and detailed features of the simulation were addressed in the earlier literature [11, 13].

3.1. Energy Balance in Laser, Wire, Deposit, and Substrate

The laser power and wire addition determine the amount of energy input into the process and consequently affect the bead geometry. For instance, the higher power results in the wider width of a deposited bead. Also, heating the wire affects the stability of the process. Therefore, a quantitative evaluation of the energy during the LMD-w process is necessary to determine the

amount of energy coming from each wire (=E_{Laser}) and laser (=E_{Wire}). The energy balance equations are given below.

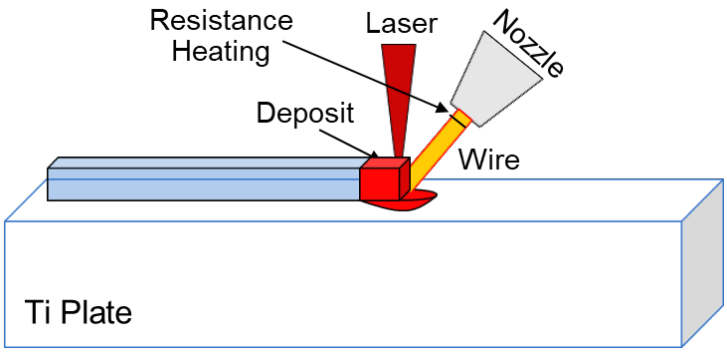

Figure 5. Schematic of laser metal deposition with wire (LMD-w) process.

$$E_{Laser} + E_{Wire} = E_{Deposit} + E_{Substrate} + E_{Loss} \quad (1)$$

$$E_{Loss} = E_{Rad.} + E_{Conv.} \quad (2)$$

The input energy stems from laser and resistance heating at the wire. The generated energy is consumed to melt the substrate (=$E_{Substrate}$) and create a deposit (=$E_{Deposit}$) on the substrate, as illustrated in Fig. 5. Some energy is lost (=E_{Loss}) by convection (=$E_{Conv.}$) and radiation (=$E_{Rad.}$) through the air given in equation 2. Based on energy conservation, the energy generated from the wire can be calculated by equation 3. A temperature rise of wire is calculated by equation 4 [14]. The predicted value can be used as a simulation input parameter. In actual printing, the wire feed rate is actively controlled to maintain a constant deposit height. For computational simplicity, the heat generated by resistance heating is incorporated into the laser heat input. The beam efficiency value is approximated from the values in the literature [11, 15, 16], and the efficiency of 70% is selected for the simulation.

$$E_{wire} = I^2 \cdot R \cdot t = \left[\int_{T_0}^{T_1} C_p \, dT\right] \cdot m \quad (3)$$

$$\Delta T_{wire} = (\rho_r \cdot I^2 \cdot l) \,/\, (v_{wire} \cdot (A_{wire})^2 \cdot C_p \cdot \rho_{den}) \quad (4)$$

where E_{wire} is the energy generated by the resistance heating of wire, I is current, R is the resistance of the wire, t is time, Cp is specific heat, T is temperature, l is the wire heating extension, v_{wire}, A_{wire}, and ρ_{den} is the feed rate, area, and density of the wire, respectively.

During the LMD-w process, the laser beam is used as a thermal energy heat source to fuse the wire and substrate. The laser beam can be considered as a point-concentrated or volumetric ellipsoidal heat source model. In this study, to accelerate the computation speed, the point-concentrated heat source is used as a heat input. It is reported that the influence of the heat

source type was not strong on the part scale temperature distribution [11]. The mathematic equation of the laser heat source is expressed by a given equation 5.

$$\dot{Q}(x,y,z,t) = \frac{2P\varphi}{abc\pi\sqrt{\pi}}\exp(-\frac{(x+v_x t)^2}{a}+\frac{y^2}{b}+\frac{z^2}{c}) \quad (5)$$

where *P* is the laser power, φ is the beam absorptance, and a, b, and c are the dimensions of heat source along x, y, and z axis, respectively. v_x is the velocity of moving the heat source.

3.2. Boundary Conditions and Build Geometry

The build geometry shown in Fig. 1 was discretized and meshed for the FEM simulation. The computation domain was created using mesh and a geometry generation toolkit CUBIT by Sandia National Laboratory. Fig. 6 shows the geometry used in the simulation. A different mesh size of 1.1 mm for the Ti plate and wall, and 5.6 mm for steel plate were used in the model for computational efficiency. Hexahedral elements with DC3D8 and C3D8R types were used for thermal and structural simulation. Since two ceramic washers were used to clamp the plates, the top and bottom surface of the washer were fully constrained in the x-, y-, and z-directions during the simulation.

Although a ceramic washer was used to minimize heat loss by conduction through the steel plate, heat conduction still occurred through the contact of the washer and the gap between the Ti-plate and steel plate. The close thermal contact is accounted for as a gap conductance condition in the simulation. The extent of this region relies on the build constraint conditions, temperature, and evolving deformation of the plate [11, 17, 18]. The values of 0.4~0.8 mW/mm^2·^{o}C at the area around the washers and 0.02~0.09 mW/mm^2·^{o}C at the other regions were used as calibration parameters in this study.

A combined heat transfer coefficient of convection and radiation was used for heat loss through the surrounding environment [19]. This equation is expressed below

$$h_{comb} = \varepsilon \cdot 24.1 \times 10^{-4} \cdot T^{1.61} \quad (6)$$

where h_{comb} is the combined heat transfer coefficient and ε is emissivity.

A simple isotropic plasticity model was used for the mechanical response. The thermo-mechanical properties were obtained from a material simulation tool called JMatPro [20] and additional literature [21, 22]. Homogeneous and temperature-dependent material properties used in the simulation are given in the appendix. The values are listed in Table 1-3 for Ti-6Al-4V, SS416, and a ceramic washer, respectively.

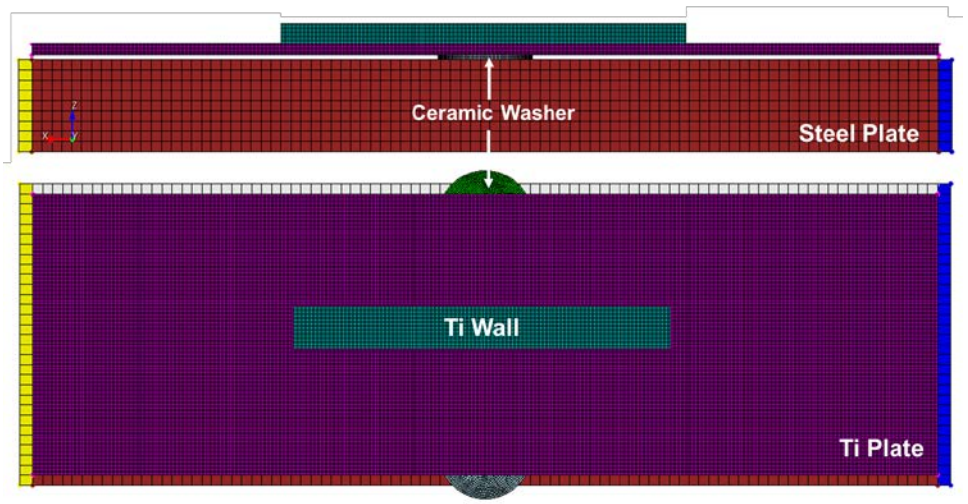

Figure 6. Build geometry of center clamped part, build 3.

4. Results

An accurate prediction of temperature profile results in better prediction in distortion since the structural analysis is sequentially coupled with the heat transfer analysis. Figure 7 shows a comparison of the predicted temperature profiles with the measured ones. The temperature values were extracted from the model time histories at the monitoring locations of T10, 15, and 18 as shown in Fig. 1(c). Generally, a higher temperature is observed at the center region (=TC15) than the temperature at the left region (=TC18) and right region (=TC10). The peak temperatures at the center of Fig. 7(b) continuously increase as the build is deposited, while the peaks at the left in Fig. 7(a) and right in Fig. 7(c) are saturated at around 1,700s~2,000s of build time. It seems that the rate of heat dissipation by conduction through the center and the sides is not identical due to the different contact conditions between the Ti plate, ceramic washer, and steel plate. Notice that the Ti plate is tied with the steel plate using steel bolts. The heat conduction rate is significantly higher at the bolts. Also, the bolts give an additional pressure to the Ti plate, washer, and steel plate. It reduces an air gap between the components and consequently leads to an increase of heat transfer through the washers. More energy is extracted from the deposit to the plate through the center, but the plate conductivity is the same. Therefore, more heat accumulated at the center plate resulting in higher temperatures. The non-uniform cooling rate between the center and side regions leads to plate distortion or *warping* as seen in Fig. 8.

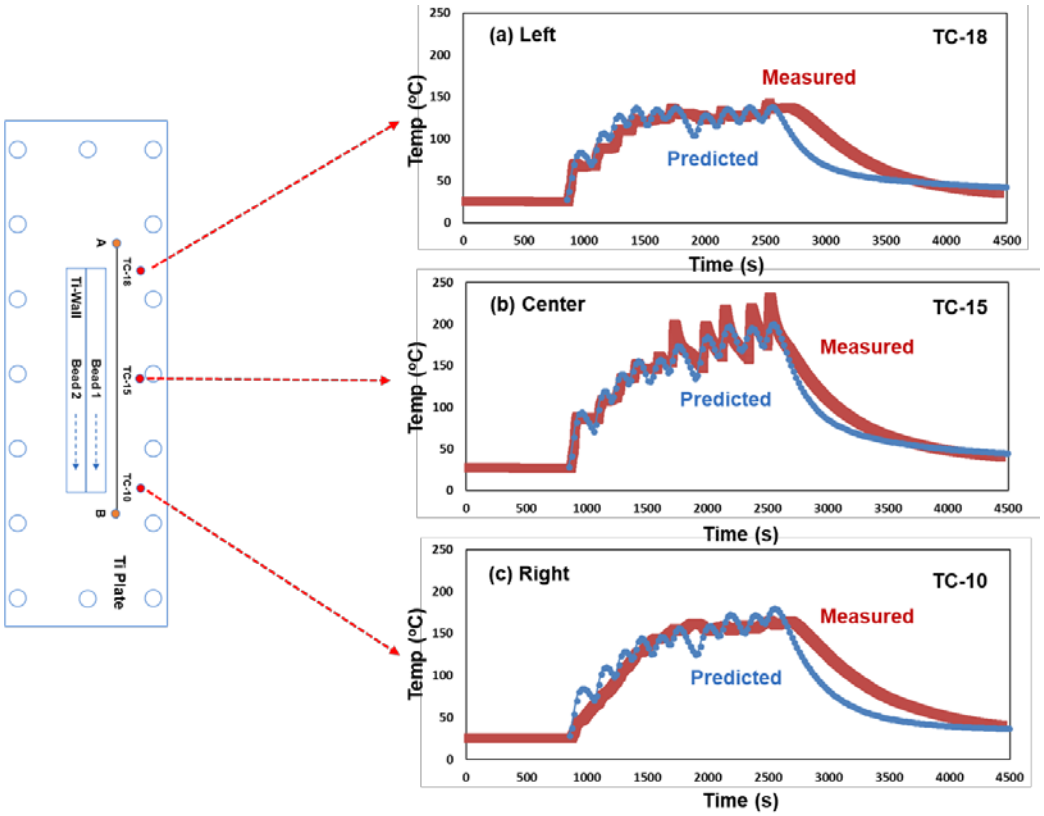

Figure 7. Validation of the predicted temperature profile with the measured data at the (a) left (=TC18), (b) center (=TC15) and (c) right (=TC10) region of the part.

The total displacement (=U) is shown in Fig. 8 at the tenth layer during cooling. It clearly shows that the Ti plate undergoes overall upward bending at the edges. The distortion features in Fig. 8 have been exaggerated by three times for visual clarity.

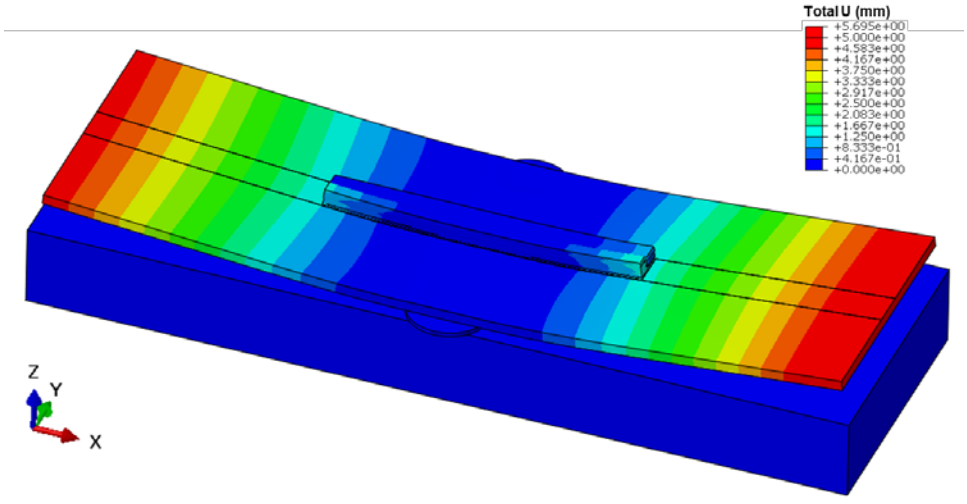

Figure 8. Total displacement of center-clamped and no-pause build at the 10th layer during cooling (Exaggerated by three times for visual clarity).

The predicted displacement is compared with the measured data at each layer in Fig 9. The plate scan was performed along the line of A-B as shown in Fig. 1(c). The red and blue lines indicate the predicted and measured data, respectively. Both experimental measurements and predicted results show asymmetric upward bending. For instance, in Figs. 9(g)-(h), the displacement value on the left is larger than the right by approximately 10%. Notice that the displacement surges by about 20% between 6^{th} and 7^{th} layer. The longest inter-layer time is found at the 6^{th} layer. There are some off values observed in the prediction. However, the displacement versus distance is generally agreed to be well with the experiment, which proves the accuracy of the proposed FEM model approach.

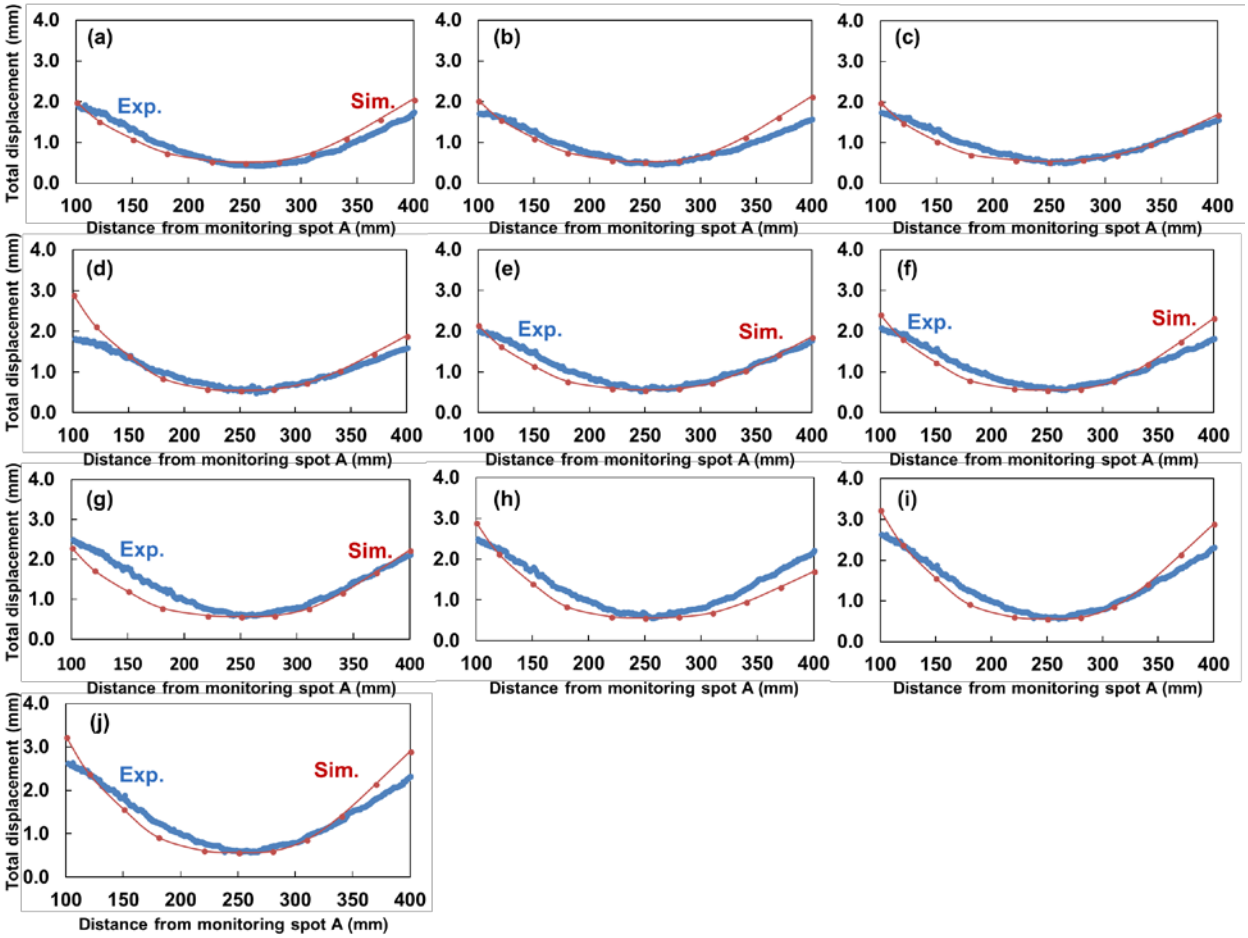

Figure 9. Validation of the predicted total displacement with the experimental data at (a) layer 1, (b) layer 2, (c) layer 3, (d) layer 4, (e) layer 5, (f) layer 6, (g) layer 7, (h) layer 8, (i) layer 9 and (j) layer 10, the displacement is measured along the scan line of A-B in Fig. 1.

Figure 10 shows the plate distortion during a heating and cooling period. Initially, the Ti-plate undergoes downward bending as the material is added onto the plate. The newly created deposit is hot and expands the volume due to large thermal expansion at the high temperatures [10, 23]. The expansion on the hot deposit wall is relatively larger than the expansion on the Ti plate such that the plate bends downward. As the part cools during the interval between layers

(i.e., inter-layer time), the expanded material shrinks and causes a strong contraction in the center region. Consequently, the plate edges are lifted upward, and this results in the plate warping. The features of upward and downward bending are repeated until the end of the process. The repeated warping feature are well captured by the structural simulation in Fig. 10(a)-(f). The magnitude of total displacement is relatively smaller at layer 1, Fig.10(b) than at layer 10, Fig. 10(f). As seen in Fig. 3(c), the inter-layer time varies with the number of layers. The magnitude of distortion seems to be closely related to the inter-layer time.

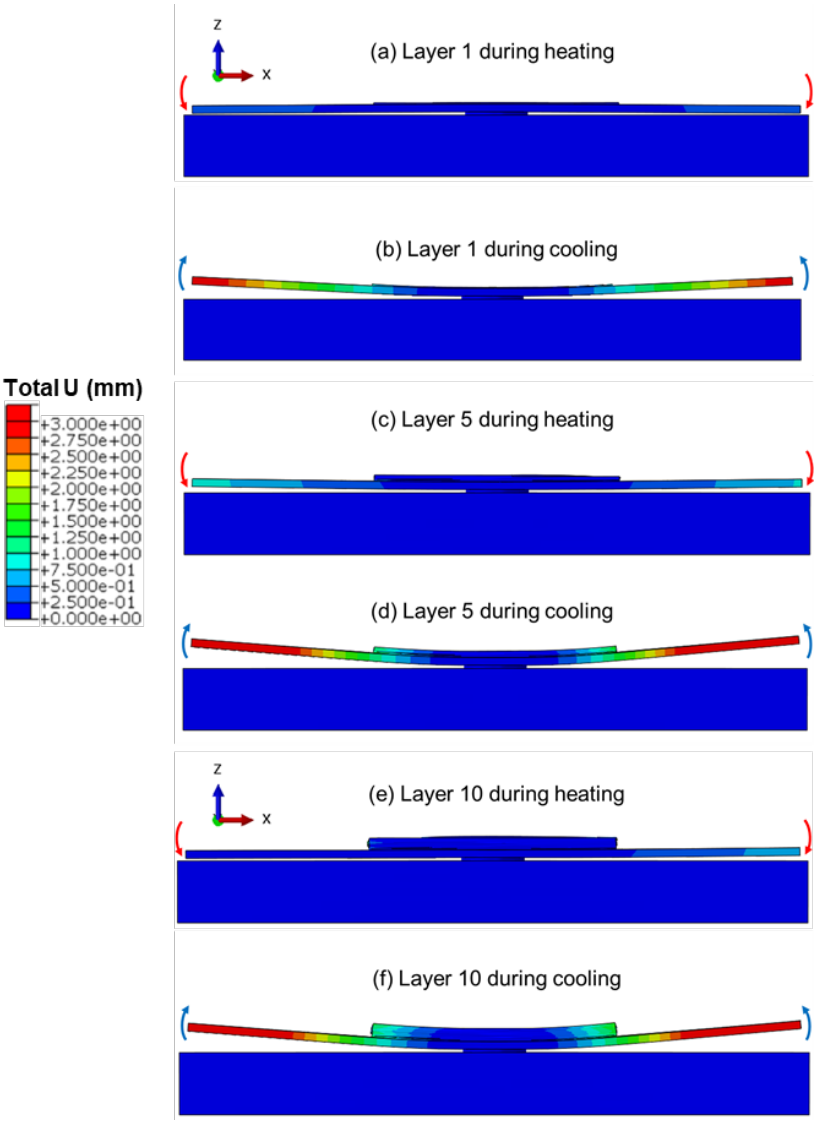

Figure 10. Repeated upward and downward plate bending over the build, the downward bending occurs during heating (a), (c) and (e) while the upward bending occurs during the cooling (b), (d) and (f).

Figure 11 shows the variation of total displacement at the 1st, 3rd, 6th, 7th, and 10th layer during cooling. At the center region, the displacement is minimal over the layers due to the clamping condition. The predicted maximum total displacement generally increases with increased build height.

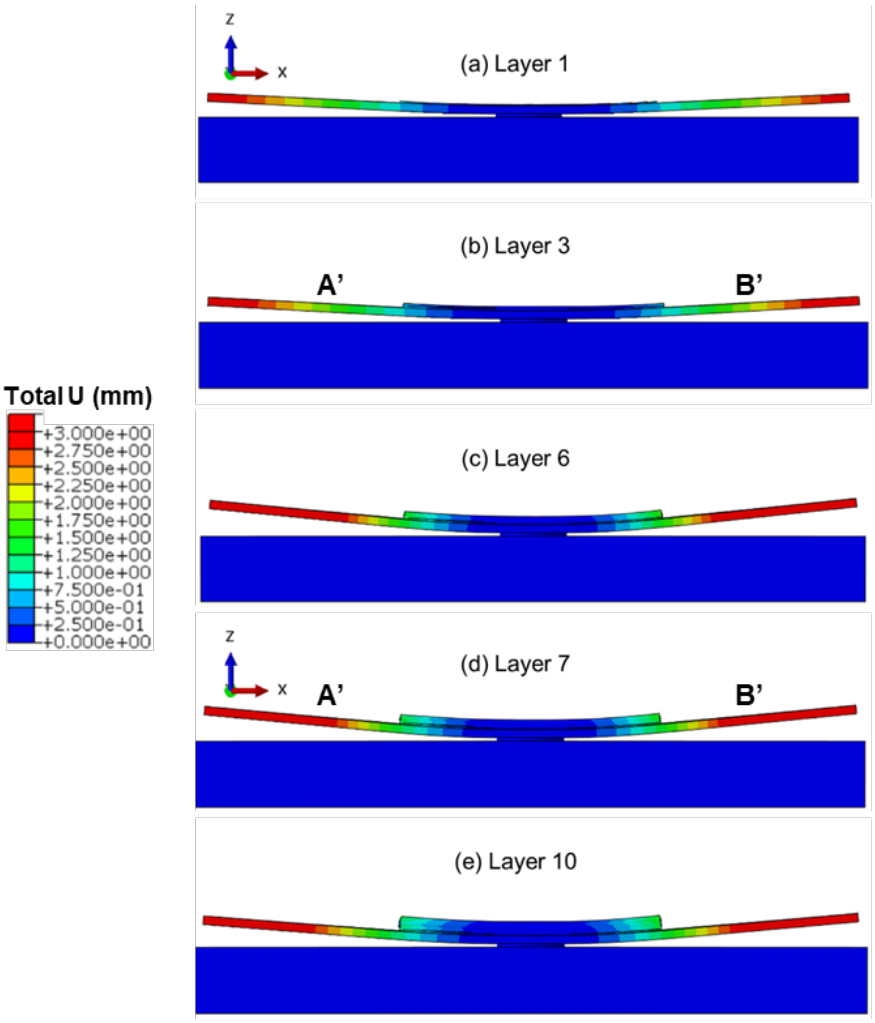

Figure 11. Variation of max. total displacement at the (a) layers 1, (b) layers 3, (c) layers 6, (d) layers 7 and (e) layers 10, the displacement generally increases over the printing process.

The variation of total displacement was obtained at 100 mm (A') and 400 mm (B') on the line of A and B in Fig. 1(c) and compared with the predicted values for quantitative analysis. The blue and orange solid lines represent the predicted results at the monitoring locations. The red squares and green rhombuses indicate the corresponding measured values. Blue cross and black triangle denote simulation outliers, which are the maximum offset values from the experiment. Overall, the displacement increases as the more layers were deposited as shown in Fig. 12(a). It has been agreed that the trend in the simulation of this experiment has an accuracy of 90% at the left and 87% at the right on average (the outliers are not included for the calculation in Fig. 12(b).). Notice that the displacement values are not identical on the A (=left) and B(=right) regions of the plate. This indicates that the distortion is asymmetric, and the plate bends more on the left side. It is likely attributed to the fact that the thermal conditions are not consistent due to the unidirectional scan direction.

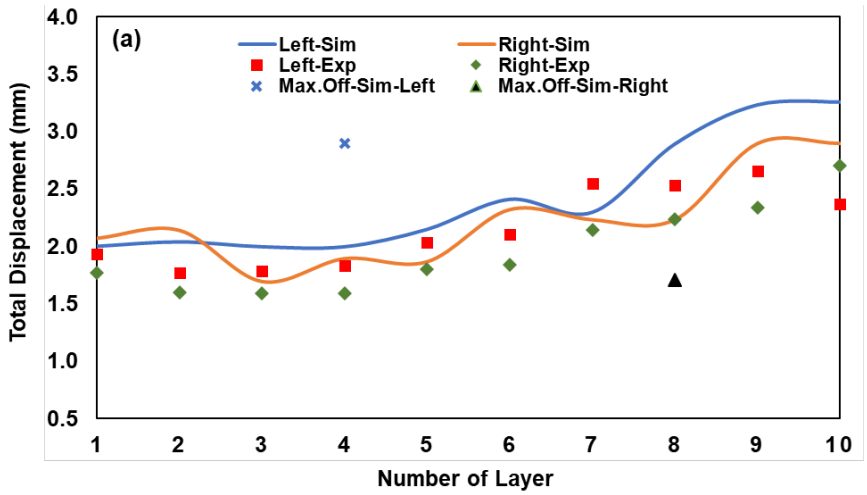

(b)

# Layer	% Match (A')	% Match (B')
1	96.5%	85.5%
2	86.6%	74.8%
3	89.6%	93.9%
4	63.3%	84.0%
5	94.8%	96.7%
6	87.3%	79.2%
7	110.9%	95.8%
8	87.5%	131.1%
9	82.2%	80.6%
10	72.5%	93.3%
Avg	**89.8%**	**87.1%**

Figure 12. Variation of total displacement at 100 mm (A') and 400 mm (B') on the line of A and B, upward trend in the prediction and experiment are well agreed. It shows that the distortion is not symmetric at the sides. The accuracy is approximately 90% and 87% at the left and right region.

5. Summary and Conclusion

In this paper, the sequentially coupled thermal-stress simulation was conducted for a large-scale LMD-w process to provide a quantitative understanding of the inter-layer cooling time on Ti plate distortion. Through the experimental and numerical investigation of the process, the following conclusions can be drawn:

- The simulation effectively captures thermally induced part oscillation of the Ti-plate during the deposition of material.
- The large-scale simulation shows about 90% accuracy in displacement prediction. It indicates that the proposed simulation provides reliable results for the LMD-w process.
- The distortion is asymmetric at the Ti- plate edges due to different thermal conditions stemming from the unidirectional scan direction.
- The inter-layer time of a couple of minutes seems not to have a considerable influence on the distortion in the large-scale part.

Although only a simple double track simulation is conducted, the modeling approach shows a potential to aid in understanding the distortion behavior during the large-scale process. Ongoing work includes an extension of the simple two beads to complex geometry, residual stress, and microstructure prediction. The heat transfer simulation needs to reduce the time step to precisely capture the temperature profiles at around the melting temperature of the material. Then, the model may be used to control microstructure and stress evolution to guarantee the desired mechanical properties in the LMD-w process.

6. Acknowledgments

The research was sponsored by the US Department of Energy, Office of Energy Efficiency and Renewable Energy, Advanced Manufacturing Office under contract DE-AC05-

00OR22725 with UT-Battelle, LLC. This work is also supported in part by Cooperative Research and Development Agreement with GKN Aerospace, under contract No. NFE-15-05725.

7. References

[1] D. Ding, Z. Pan, D. Cuiuri, H. Li, Wire-feed additive manufacturing of metal components: technologies, developments and future interests, *The International Journal of Advanced Manufacturing Technology*, 2015, 81, pp.465-481.
[2] B.A. Szost, S. Terzi, F. Martina, D. Boisselier, A. Prytuliak, T. Pirling, M. Hofmann, D.J. Jarvis, A comparative study of additive manufacturing techniques: Residual stress and microstructural analysis of CLAD and WAAM printed Ti–6Al–4V components, *Materials & Design*, 2016, 89, pp.559-567.
[3] W.E. Frazier, Metal additive manufacturing: a review, *Journal of Materials Engineering and Performance*, 2014, 23, pp.1917-1928.
[4] M.P. Mughal, H. Fawad, R. Mufti, Finite element prediction of thermal stresses and deformations in layered manufacturing of metallic parts, *Acta Mechanica*, 2006, 183, pp.61-79.
[5] H. Zhao, G. Zhang, Z. Yin, L. Wu, Effects of Interpass Idle Time on Thermal Stresses in Multipass Multilayer Weld-Based Rapid Prototyping, *Journal of Manufacturing Science and Engineering*, 2013, 135, pp.011016-011016-6.
[6] P. Aggarangsi, J.L. Beuth, Localized preheating approaches for reducing residual stress in additive manufacturing, Proc. SFF Symp., Austin, 2006, pp. 709-720.
[7] J. Ding, P. Colegrove, J. Mehnen, S. Williams, F. Wang, P.S. Almeida, A computationally efficient finite element model of wire and arc additive manufacture, *The International Journal of Advanced Manufacturing Technology*, 2014, 70, pp.227-236.
[8] J. Ding, P. Colegrove, J. Mehnen, S. Ganguly, P.S. Almeida, F. Wang, S. Williams, Thermo-mechanical analysis of wire and arc additive layer manufacturing process on large multi-layer parts, *Computational Materials Science*, 2011, 50, pp.3315-3322.
[9] F. Montevecchi, G. Venturini, N. Grossi, A. Scippa, G. Campatelli, Idle time selection for wire-arc additive manufacturing: A finite element-based technique, *Additive Manufacturing*, 2018, 21, pp.479-486.
[10] J. Heigel, P. Michaleris, E. Reutzel, Thermo-mechanical model development and validation of directed energy deposition additive manufacturing of Ti–6Al–4V, *Additive manufacturing*, 2015, 5, pp.9-19.
[11] S. Simunovic, A. Nycz, M.W. Noakes, C. Chin, V. Oancea, Process Modeling and Validation for Metal Big Area Additive Manufacturing, *NAFEMS World Congress, Stockholm, Sweden*, 2017, pp.1-17.
[12] ABAQUS Analysis User's Manual, Dassault Systémes Simulia Corp, Providence, RI, USA, 2017.
[13] S. Tripathy, C. Chin, T. London, U. Ankalkhope, V. Oancea, Process Modeling and Validation of Powder Bed Metal Additive Manufacturing, *NAFEMS World Congress, Stockholm, Sweden*, 2017.
[14] H. Wei, Y. Zhang, L. Tan, Z. Zhong, Energy efficiency evaluation of hot-wire laser welding based on process characteristic and power consumption, *Journal of Cleaner Production*, 2015, 87, pp.255-262.
[15] F. Montevecchi, G. Venturini, A. Scippa, G. Campatelli, Finite element modelling of wire-arc-additive-manufacturing process, *Procedia CIRP*, 2016, 55, pp.109-114.

[16] J. DuPont, A. Marder, Thermal efficiency of arc welding processes, *Welding Journal-Including Welding Research Supplement*, 1995, 74, pp.406s.
[17] X. Bai, H. Zhang, G. Wang, Improving prediction accuracy of thermal analysis for weld-based additive manufacturing by calibrating input parameters using IR imaging, *The International Journal of Advanced Manufacturing Technology*, 2013, 69, pp.1087-1095.
[18] N. Pépe, S. Egerland, P.A. Colegrove, D. Yapp, A. Leonhartsberger, A. Scotti, Measuring the process efficiency of controlled gas metal arc welding processes, *Science and Technology of Welding and Joining*, 2011, 16, pp.412-417.
[19] J. Goldak, A. Chakravarti, M. Bibby, A new finite element model for welding heat sources, *Metallurgical transactions B*, 1984, 15, pp.299-305.
[20] N. Saunders, U.K.Z. Guo, X. Li, A.P. Miodownik, J.-P. Schillé, Using JMatPro to model materials properties and behavior, *JOM*, 2003, 55, pp.60-65.
[21] B. Babu, L.-E. Lindgren, Dislocation density based model for plastic deformation and globularization of Ti-6Al-4V, *International Journal of Plasticity*, 2013, 50, pp.94-108.
[22] http://www.associatedceramics.com/zirconia.php.
[23] E.R. Denlinger, J.C. Heigel, P. Michaleris, T. Palmer, Effect of inter-layer dwell time on distortion and residual stress in additive manufacturing of titanium and nickel alloys, *Journal of Materials Processing Technology*, 2015, 215, pp.123-131.

8. Appendix

Table 1. Material properties of Ti plate and wall used in the model [20, 21]

Temp (°C)	Density	Cond.	Specific	Temp (°C)	Exp.	E	Poisson Ratio	Temp (°C)	Yield	Plastic Strain
110	4.42	7.2	5.6	93	12.1	101	0.33	20	1000	0.00
								20	1200	0.03
210		8.8	5.8	205	12.5	94	0.33	20	1300	0.08
310		10.4	6.0	315	12.9	88	0.33	20	1320	0.13
410		11.9	6.2	425	13.3	82	0.33	400	680	0.00
								400	850	0.03
510		13.5	6.5	540	13.8	77	0.33	400	900	0.08
610		15.1	6.7	650	14.2	72	0.33	400	910	0.13
710		16.6	6.9	710	14.4	67	0.33	600	700	0.00
								600	630	0.08
810		18.2	7.1	870	15.0	62	0.33	600	620	0.18
910		19.8	7.3	* Latent Heat: 2.86 e+11, 1604 °C (S), 1650 °C (L) *DENSITY: e-9 tonne / mm^3 *SPECIFIC HEAT: e+8 mJ / (tonne.C) *CONDUCTIVITY: mW / (mm.C) *EXPANSION: e-6 /°C *ELASTIC: e+3 MPa *PLASTIC: MPa *Latent Heat: mJ / tonne				600	610	0.28
1010	4.34	21.4	7.5					800	200	0.00
1110		22.9	7.8					800	210	0.08
1210		24.5	8.0					800	200	0.18
1310		23.6	6.9					800	195	0.28
1410		24.8	7.1					1100	19	0.00
1510		26.1	7.3					1100	18	0.08
1610		27.4	7.5					1100	18	0.18
								1100	18	0.28

Table 2. Material properties of steel (SS416) plate used in the model [20]

Temp (°C)	Density	Cond.	Specific	Temp(°C)	Exp.	E	Poisson Ratio	Yield
110		18.4	4.8	93	12.1	210	0.33	354
210		19.6	5.2	205	12.5	203	0.33	306
310		21.0	5.7	315	12.9	194	0.33	279
410		22.5	6.2	425	13.3	183	0.33	258
510		23.8	7.0	540	13.8	169	0.33	246
610		24.8	8.1	650	14.2	155	0.33	237
710		25.6	10.1	710	14.4	146	0.33	167
810	7.73	26.5	7.4	870	15.0	123	0.33	95
910		27.5	7.0	* Latent Heat: 2.72 e+11, 1265 °C (S), 1500 °C (L) *DENSITY: e-9 tonne / mm^3 *SPECIFIC HEAT: e+8 mJ / (tonne.C) *CONDUCTIVITY: mW / (mm.C) *EXPANSION: e-6 /°C, *ELASTIC: e+3 MPa *PLASTIC: MPa, *Latent Heat: mJ / tonne				
1010		28.6	6.9					
1110		29.8	7.0					
1210		30.9	7.1					
1310		32.0	7.4					
1410		33.1	8.5					
1510		32.5	-					

Table 3. Material properties of ceramic washer used in the model [22]

Temp (°C)	Density	Cond.	Specific	Exp.	E	Poisson Ratio	Yield
25	0.24	2.5	4.50	12.17	207	0.33	345
*DENSITY: e-9 tonne / mm^3, *SPECIFIC HEAT: e+8 mJ / (tonne.C), *CONDUCTIVITY: mW / (mm.C), *EXPANSION: e-6 /°C *ELASTIC: e+3 MPa, *PLASTIC: MPa							